Controlling the optical dipole force for molecules with field-induced alignment

S. M. Purcell and P. F. Barker
Department of Physics and Astronomy, University College London, London, WC1E 6BT, United Kingdom
(Received 22 June 2010; published 28 September 2010)

We measure the role of field-induced alignment on the dipole force for molecules using a single focused nonresonant laser beam. We show that through the alignment process we can modify the effective polarizability by field polarization and thus control the center-of-mass motion of the molecule. We observe a maximum change of 20% in the dipole force on CS_2 molecules when changing from linearly to circularly polarized light. Additionally, the effect of the dipole force on different vibrational states is also studied.

DOI: 10.1103/PhysRevA.82.033433 PACS number(s): 37.10.Vz, 42.50.Hz, 33.15.−e, 42.50.Tx

I. INTRODUCTION

Optical forces have become prevalent in the control of the center-of-mass motion of atoms and molecules. Laser cooling, atom optics [1], Bose-Einstein condensation (BEC) [2,3], and the creation of ultracold atomic species by association all rely on conservative and/or dissipative optical forces. The manipulation of molecular degrees of freedom by optical means is, however, less well developed, particularly for complex molecular species. This is due to the complex energy structure of these species which largely precludes laser cooling. In addition, the near-resonant enhancement of the dipole force, which is often used to manipulate cold atomic species using near-infrared and visible laser sources, would for many molecules, require lasers in the ultraviolet and vacuum ultraviolet which are generally not available.

Another route for manipulating molecular or atomic species is to use strong optical fields that are far from resonance. Here, well-developed, high-intensity pulsed laser sources in the infrared are available and capable of generating large optical forces that can significantly change the center-of-mass motion of molecules on the nanosecond time scale. Using nanosecond, intense ($\approx 10^{11}$ W cm^{-2}) optical fields, confinement of room temperature molecular gases [4] has been demonstrated. In addition, a molecule prism [5], a lens [6–9], and a molecular decelerator and accelerator [10] have been realized.

For a molecule irradiated by nonresonant optical radiation, an induced dipole is created which interacts with the field that created it. The force is proportional to the gradient of the product of the polarizability and the square of the electric field. Of particular interest for the manipulation of molecules by the dipole force is that many molecules and larger particles have a nonspherical shape and therefore different polarizability components along each molecular axis. Because of this, the induced dipole moment and thus the dipole force is dependent on the orientation of the molecule with respect to the field polarization. However, a variation in the dipole force due to this effect is not typically observed due to the averaging of the random orientation of molecules in a gas.

A method to control the orientation or the alignment of molecules with the optical field polarization would allow the observation of this orientational dependence of the optical dipole force. Such alignment is produced by strong, nonresonant optical fields [11,12], and this has been an area of intense study over the last ten years. This alignment has been observed and occurs when one or more of the body-fixed molecular axes is brought into alignment with a laboratory fixed axis [13,14]. It occurs because of differences in the induced dipole moment along each of the molecular axes. Because the induced dipole is proportional to the polarizability, a torque is created, rotating the molecule until the highest axis of polarizability is aligned with the electric field. When a short, typically subnanosecond pulsed laser is used, a rotational wave packet in the ground state is created, and the alignment occurs in a series of revivals after the optical field has been turned off. This allows the molecular axes to be studied in the laboratory frame and under field-free conditions. This type of alignment has also been observed and is termed nonadiabatic alignment [15]. It has many applications which have been experimentally demonstrated, such as in tomographic imaging of molecular orbitals [16], photodissociation studies [17], and chemical reaction dynamics [18,19]. When pulsed nanosecond lasers are used to induce the molecular alignment, the electric-field envelope changes slowly compared to the rotational period of the molecule, and this type of alignment is termed adiabatic. Under this condition, the molecule behaves classically, and the observed alignment follows the electric-field envelope and disappears when the field is turned off [20].

In this paper, we describe in detail the use of strong optical fields to simultaneously control both the center-of-mass motion as well as the rotational motion of a molecule. This is accomplished by modifying the optical dipole force for carbon disulfide (CS_2) molecules using a single focused laser beam [21]. This modification occurs because the alignment of the molecule with respect to the electric-field polarization changes the molecule's effective polarizability when compared to the random molecular orientation in a gas. In Sec. II we describe the optical dipole force for aligned linear molecules, while in Sec. III we describe the experimental setup and measurements made in a molecular beam using linearly and circularly polarized light. Finally, in Sec. IV, we describe measurements to study the dipole force on vibrationally active molecules.

II. THEORY

A. Adiabatic alignment

The electric field of optical radiation can be represented by $\mathbf{E}(t) = \frac{1}{2}\hat{\boldsymbol{\varepsilon}} E_0 \exp(i\omega t) + \text{c.c.}$, where $\hat{\boldsymbol{\varepsilon}}$ is a unit vector of the field polarization, E_0 is the field amplitude, and ω its frequency. This field induces a dipole moment in a molecule and, when

detuned far from any single-photon resonances, is capable of inducing nonresonant Raman transitions between rotational levels. When the optical frequency is much greater than the rotational frequency, the interaction is well approximated by the square of the optical field and the Raman polarizability tensor $\boldsymbol{\alpha}_{J,J'}(\omega_l)$, expressed in the molecular frame. In the ground state, the polarizability is primarily constructed from the electronic part of the wave function and varies little with rotational quantum number, thus it is reasonable to replace the Raman polarizability tensor with the static-field polarizability tensor $\boldsymbol{\alpha}$. This interaction is represented by an effective Hamiltonian which describes the ac Stark shift in a molecule and is written [22,23]

$$V(r,t) = -\tfrac{1}{4}\alpha_{\text{eff}} E(r,t)^2, \tag{1}$$

where α_{eff} is an effective polarizability determined by the rotation of the body-fixed molecule axis into the laboratory frame where the laser polarization is best expressed. The molecule's alignment is expressed in spherical coordinates, and we define a laboratory fixed Z axis for each laser polarization. We follow the convention of choosing Z to be parallel with the electric-field vector for linearly polarized light and parallel to the propagation direction for circularly polarized light. For a linear molecule, the effective polarizability for linearly and circularly polarized light is [24,25]

$$\alpha_{\text{eff}} = \Delta\alpha \cos^2\theta_l + \alpha_\perp, \tag{2}$$

and

$$\alpha_{\text{eff}} = \tfrac{1}{2}(\alpha_{||} + \alpha_\perp - \Delta\alpha \cos^2\theta_c), \tag{3}$$

respectively, where the constants $\Delta\alpha = \alpha_\parallel - \alpha_\perp$, and $\alpha_\parallel$ and $\alpha_\perp$ are the parallel and perpendicular polarizabilities with respect to the molecular symmetry axis. We define $\theta_{l,c}$ as the angle between the laboratory fixed Z axis and the bond axis for each polarization. Figure 1 shows the alignment of a molecule with linearly and circularly polarized light. In Fig. 1(a), linearly polarized light and the electric-field vector (green) lie parallel with the laboratory fixed Z axis. We label θ_l as the angle between the Z axis and the molecular bond axis. In Fig. 1(b), circularly polarized light is shown. The angle θ_c is

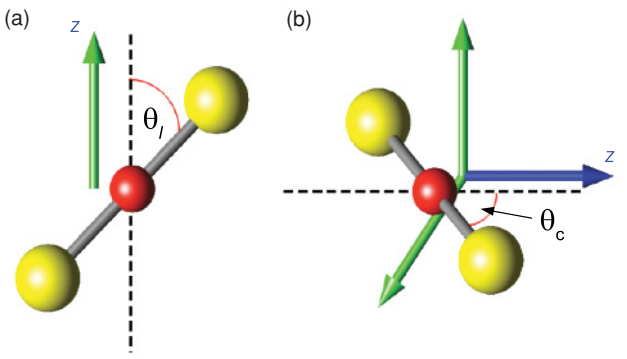

FIG. 1. (Color online) The alignment of CS_2 with (a) linearly and (b) circularly polarized light. For linearly polarized light, the polarization vector lies parallel to the electric field (green) along the space fixed direction Z. The Z direction for circularly polarized light is chosen to be parallel to the propagation direction (blue), but perpendicular to the plane of the radiation (green).

the angle between the propagation direction and the molecular symmetry axis. In all linear molecules, $\alpha_{||} > \alpha_\perp$; and for linearly polarized light, the $\alpha_{||}$ component exerts a greater torque on the molecule, and complete alignment corresponds to $\theta_l = 0^\circ$ and $\alpha_{\text{eff}} = \alpha_{||}$. For circularly polarized light, the molecule is confined to the electric-field plane with $\theta_c = 90^\circ$. The electric-field components are equal in the plane, and so there is an average of the polarizability components along each axis of the molecule. When complete alignment occurs, $\alpha_{\text{eff}} = \frac{\alpha_{||}+\alpha_\perp}{2}$. To calculate the effective polarizability of the molecule for both laser polarizations, the expectation value $\langle\cos^2\theta_{l,c}\rangle$ is calculated as a function of optical intensity.

The Schrödinger equation is used to calculate the expectation values from the Hamiltonian $H(t) = H_0 + V(t)$, where $H_0 = B\mathbf{J}^2$ is the field-free Hamiltonian of the rigid rotor, $\mathbf{J}^2$ is the squared angular momentum operator, and $B = 0.109\,\text{cm}^{-1}$ is the rotational constant of CS_2 [26]. The properties of the rigid rotor equation are well known. Its solutions are the spherical harmonics [27,28], and the energy of rotation of the molecule is $E_J = BJ(J+1)$. Centrifugal distortion effects are not taken into account in the calculation. Molecular vibrations are also ignored. To calculate high rotational temperatures, an approximation is made that in dipole force experiments the electric-field envelope changes slowly compared to the carbon disulfide rotational dynamics. When this condition is met, the alignment adiabatically follows the electric-field envelope [24]. Quantum mechanically, the eigenvalues of the molecule in adiabatic alignment always correlate with the field-free stationary Schrödinger equation dressed by an electric field. The adiabatic dynamics allow the "long pulse" approximation [29] to be used, which reduces the Schrödinger equation to an eigenvalue problem. To check our calculations, the time-dependent Schrödinger method [30,31] was also used to calculate the rotational dynamics up to a rotational temperature of 30 K, and complete agreement was found between the methods.

In both methods, the complete rotational wave function $\Psi_{\tilde{J},M}(t)$ was represented as a superposition of field-free rotor states $\Psi_{\tilde{J},M}(t) = \sum_{J,M} C_{J,M}(t)|J,M\rangle$, where $C_{J,M}(t)$ are the time-dependent coefficients in the expansion and $|J,M\rangle$ are the spherical harmonics. The labels J and M refer to the quantum numbers for the squared angular momentum operator and its projection onto the Z axis, respectively. The label $\tilde{J}$ represents the field-free state J, which has been perturbed by the optical field and is constructed from field-free $|J,M\rangle$ states. For the time-dependent method, substituting $\Psi_{\tilde{J},M}(t)$ into the Schrödinger equation yields the equations of motion for the molecule. Written in dimensionless form, we find

$$i\frac{d}{dn}C_{J,M}(n) = \sum_{J',M'} C_{J',M'}(n)\langle J,M|\frac{H(n)}{B}|J',M'\rangle, \tag{4}$$

where reduced units of time have been used with $t = \frac{\hbar}{B}n$ ($\frac{\hbar}{B} = 49$ ps). This equation is reduced to a series of coupled differential equations, which has been solved frequently in the literature under both adiabatic and nonadiabatic conditions [13,30–32]. Additionally, the matrix elements of the operator $H(n)$ are the same for linearly and circularly polarized light and are calculated from the recursive relations of the spherical

harmonics [31,33]. For the time-independent Schrödinger equation, we solve the dimensionless rigid rotor equation

$$\frac{H}{B}\Psi_{\tilde{J},M} = \frac{\lambda_{\tilde{J},M}}{B}\Psi_{\tilde{J},M}, \tag{5}$$

where $\lambda_{\tilde{J},M}$ is the eigenvalue of the perturbed system. Evaluating Eq. (5), we find for circularly polarized light

$$\begin{aligned}\frac{\lambda_{\tilde{J},M}}{B}C_{J,M} = {} & C_{J,M}[J(J+1) - \omega_{\perp} - \omega_{\parallel}] \\ & + C_{J-2,M}\Delta\omega\langle J,M|\cos^2\theta_l|J-2,M\rangle \\ & + C_{J,M}\Delta\omega\langle J,M|\cos^2\theta_l|J,M\rangle \\ & + C_{J+2,M}\Delta\omega\langle J,M|\cos^2\theta_l|J+2,M\rangle. \end{aligned} \tag{6}$$

A similar expression is obtained for linearly polarized light. We have introduced the parameters $\Delta\omega = \frac{\Delta\alpha E_0^2 I}{8B}$ and $\omega_{\parallel,\perp} = \frac{\alpha_{\parallel,\perp}E_0^2 I}{8B}$. An electric field of $E_0 = 2.746 \times 10^9$ V m^{-1} is used, corresponding to an intensity of 10^{12} W cm^{-2}. A dimensionless variable I is used to vary the strength of the interaction in order to calculate the expansion coefficients for different optical intensities. Equation (6), written in matrix form, can be diagonalized to determine the expansion coefficients $C_{J,M}$. The expectation value $\langle\cos^2\theta_{l,c}\rangle_{J,M}$ is then determined from the expansion coefficients [32]

$$\langle\cos^2\theta_{l,c}\rangle_{\tilde{J},M} = \sum_{J,M,J',M'} C^*_{J,M}C_{J',M'}\langle J,M|\cos^2\theta_{l,c}|J',M'\rangle. \tag{7}$$

The atoms in CS_2 have zero nuclear spin, and exchange of the sulfur atoms means the wave function is unchanged. As the ground state of carbon disulfide has $\sum_g^+$ structure, only even rotational levels are allowed in the ground state. The effects of rotational temperature are determined by assuming that a Boltzmann distribution of the rotational levels is maintained during the supersonic expansion, although in certain conditions this is not always the case [34]. The expectation value $\langle\cos^2\theta_{l,c}\rangle_{\tilde{J},M}$ for each perturbed rotational level $\Psi_{\tilde{J},M}$ is averaged with weightings according to a Boltzmann distribution:

$$\begin{aligned}\langle\cos^2\theta_{l,c}\rangle = {} & Q^{-1}\sum_J \exp\left(\frac{-BJ(J+1)}{k_bT_R}\right) \\ & \times \sum_{M=-J}^{J}\langle\cos^2\theta_{l,c}\rangle_{\tilde{J},M}, \end{aligned} \tag{8}$$

where k_b is Boltzmann's constant, T_R the rotational temperature, and Q the rotational partition function [31,35]

$$Q = \sum_J (2J+1)\exp\left(\frac{-BJ(J+1)}{k_bT_R}\right). \tag{9}$$

By inserting the thermally averaged expectation values $\langle\cos^2\theta_{l,c}\rangle$ into Eqs. (2) and (3), respectively, we now calculate the thermally averaged polarizabilities, indicated by adding a bar to the notation for the effective polarizability $\bar{\alpha}_{\text{eff}}$. This function can now be used to calculate the properties of aligned molecules in nonresonant optical fields.

Figure 2 shows the key features of adiabatic alignment. Figures 2(a) and 2(b) were calculated using the time-dependent

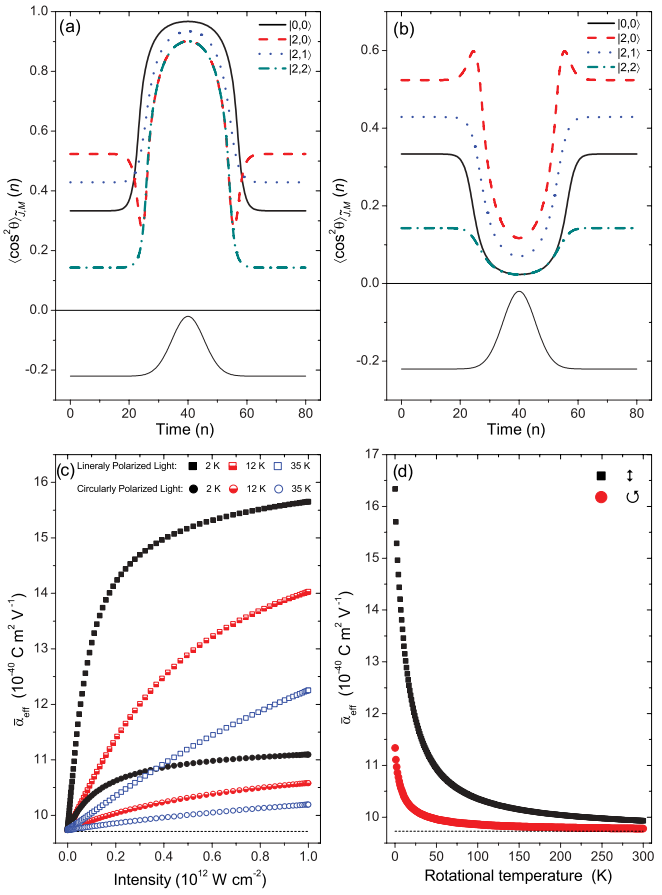

FIG. 2. (Color online) (a) and (b) show the alignment of the molecular symmetry axis of CS_2 with the Z direction calculated using the time-dependent Schrödinger equation in reduced units of time. The intensity envelope is shown at the bottom of each graph (solid thin line) and has a FWHM of 0.64 ns. The initial rotational states being perturbed in both graphs are $|0,0\rangle$ (solid line, black), $|2,0\rangle$ (dashed line, red), $|2,1\rangle$ (dotted line, blue), and $|2,2\rangle$ (dash-dotted line, dark green). (c) The effective polarizability as a function of optical intensity is shown for linearly (squares) and circularly (circles) polarized light for three rotational temperatures: 2 K (solid squares or circles, black), 12 K (half-full squares or circles, red), and 35 K (empty squares or circles, blue). (d) The effective polarizability of linearly (squares, black) and circularly (circles, red) polarized light is shown as a function of temperature at $I_0 = 5.7 \times 10^{11}$ W cm^{-2} up to room temperature. The average polarizability of CS_2 is also shown on Figs. (c) and (d) for comparison (horizontal dashed line).

method shown in Eq. (4) for linearly and circularly polarized light. The peak intensity is 10^{12} W cm^{-2}. The intensity envelope is shown at the bottom of each figure (dashed line) and has a full width at half maximum (FWHM) of 0.64 ns or $n = 13$ in reduced units. The rotational states shown in Figs. 2(a) and 2(b) are $|\tilde{0},0\rangle$ (black), $|\tilde{2},0\rangle$ (red), $|\tilde{2},1\rangle$ (dark blue), and $|\tilde{2},2\rangle$ (light blue). Both (a) and (b) show confinement of the angular motion with $\langle\cos^2\theta_l\rangle \to 1$ and $\langle\cos^2\theta_c\rangle \to 0$ for all rotational states. Rotational states with higher J generally exhibit less alignment, since they have more rotational energy and are harder to perturb from their field-free orientation. For linearly polarized light, the molecular alignment generally decreases with increasing $|M|$. This is explained by considering the wave

function of the unperturbed rotor. Low $|M|$ ($|M| \approx 0$) states have their probability distribution localized closer to the Z axis and so they are already partially aligned in the Z direction. By comparison, a high $|M|$ ($|M| \approx J$) state is partially aligned perpendicular to the Z direction, reducing the obtainable alignment. However, under field-free conditions, there is no defined laboratory frame Z direction, and a complete rotational manifold, where all of the field-free $\langle \cos^2 \theta_{l,c} \rangle$ values of a particular J state are averaged, is always $\langle \cos^2 \theta_{l,c} \rangle = 1/3$.

Figure 2(c) shows the effective polarizability for different rotational temperatures using linearly and circularly polarized light. Linearly polarized light is indicated by the solid lines and circularly polarized light by the dashed lines. The horizontal dashed line indicates the average polarizability of CS_2 with $\alpha_{av} = \frac{1}{3}(\alpha_{\parallel} + 2\alpha_{\perp}) = 9.73 \times 10^{-40}$ C m^2 V^{-1}. It can be seen that the effective polarizability for linearly polarized light rapidly increases with optical intensity. As expected from Fig. 1(b), circularly polarized light has a lower effective polarizability for the same optical intensity compared to linearly polarized light. For both polarizations, the molecules eventually reach a saturation intensity where increasing the optical intensity further does not strongly increase alignment. This saturation intensity is reached quite rapidly, and typical peak intensities in dipole force experiments are above this threshold. Figure 2(d) shows the effective polarizability for linearly (black) and circularly polarized light (red) up to $T_R = 300$ K with a constant intensity of 5.7×10^{11} W cm^{-2}. The horizontal line shows the average polarizability of CS_2. At high temperatures, the difference in effective polarizability between the laser polarizations is significantly reduced, which highlights the importance of achieving a rotationally cold molecular beam.

B. Alignment-dependent dipole forces

A typical dipole force experiment using intense pulsed fields is illustrated in Fig. 3. Two laser beams perpendicular to a molecular beam are focused onto the x-y plane inside a time-of-flight mass spectrometer (TOFMS). The IR beam (red) provides the nonresonant optical field and the blue beam is the probe, which ionizes the molecules. The ions are accelerated by a static electric field and their time-of-flight (TOF) is recorded using a microchannel plate (MCP) detector. The flat green arrows on the diagram indicate the direction of the dipole force due to the focused nonresonant laser beam. Forces along the x direction cause acceleration and deceleration, while forces along the y axis cause focusing of the molecular beam.

The dipole force is determined from the negative spatial gradient of the ac Stark shift shown in Eq. (1). The amplitude of the electric field E_0 is first expressed using the intensity of the field with $E_0(t) = \sqrt{\frac{2I_0 g(t)}{c\varepsilon_0}}$, where c and ε_0 are the speed of light and permittivity of free space, respectively, and $g(t)$ is the pulse envelope of the optical field. For a focused Gaussian laser beam, we include a spatial distribution $I(r)$ on the x-y plane with $r^2 = x^2 + y^2$. The ac Stark shift is

$$V(r,t) = -\frac{g(t)I_0}{2c\epsilon_0}\bar{\alpha}_{\text{eff}}(I,r)I(r). \tag{10}$$

The thermally averaged effective polarizability for linearly or circularly polarized light is $\bar{\alpha}_{\text{eff}}(I,r)$ and is a function of

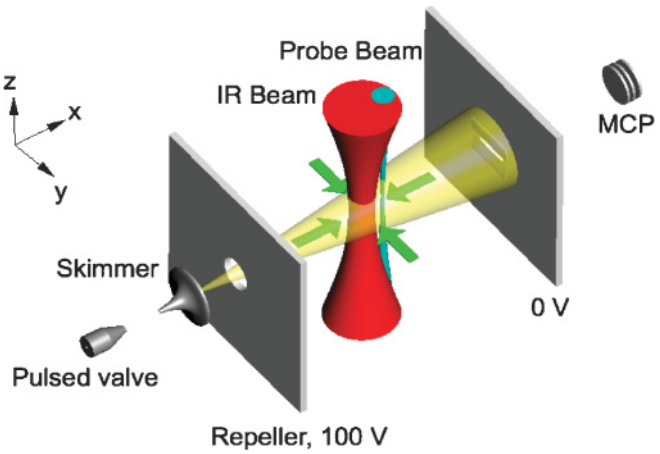

FIG. 3. (Color online) Experimental setup to measure the velocity of CS_2 molecules accelerated and decelerated by the dipole force in a time-of-flight mass spectrometer. The molecular beam propagates along the x axis, where it is crossed by a focused nonresonant laser beam (colored red). The molecules experience a radial force in the x and y directions, shown as the green arrows. The changes along the x axis are detected by ionizing the molecules using a probe beam (colored blue) and recording their time of flight.

intensity. This is in turn dependent on position and time. By fitting a curve for multiple rotational temperatures to $\bar{\alpha}_{\text{eff}}(I,r)$ shown in Fig. 2(c), an analytical form of $\bar{\alpha}_{\text{eff}}(I,r)$ can be found. Thus for a given rotational temperature over the range of calculated intensities, we may determine the alignment at any time during the laser pulse and at any spatial location. The dipole force on a polarizable molecule at a position r from the center of the IR field is $F(r,t) = -\nabla V(r,t)$. From Eq. (10)

$$\begin{aligned} F(r,t) &= \frac{g(t)I_0}{2c\epsilon_0}\nabla[\bar{\alpha}_{\text{eff}}(I,r)I(r)] \\ &= \frac{g(t)I_0}{2c\epsilon_0}[\bar{\alpha}_{\text{eff}}(I,r)\nabla I(r) + \nabla\bar{\alpha}_{\text{eff}}(I,r)I(r)]. \end{aligned} \tag{11}$$

The Gaussian focus on the x-y plane is defined by an e^{-2} waist radius ω and has the form $I(r) = \exp(\frac{-2r^2}{\omega^2})$. In our experiments, the dipole force is measured along the x axis which corresponds to acceleration and deceleration of the molecular beam. This is indicated by the green arrows parallel to the molecular beam in Fig. 3. The intensity dependence of the ensemble effective polarizability $\bar{\alpha}_{\text{eff}}(I,r)$ may be written

$$\nabla\bar{\alpha}_{\text{eff}}(I,r) = \frac{d\bar{\alpha}_{\text{eff}}(I,r)}{dI}\nabla I(r). \tag{12}$$

Considering only the x axis, where $\nabla I(x) = \frac{-4x}{\omega^2}\exp(\frac{-2x^2}{\omega^2})$, the effects of molecular alignment on the dipole force can be expressed as

$$\begin{aligned} F(x,t) = &-\frac{2xg(t)I_0}{c\epsilon_0\omega^2}\exp\left(\frac{-2x^2}{\omega^2}\right) \\ &\times\left[\bar{\alpha}_{\text{eff}}(I) + \frac{d\bar{\alpha}_{\text{eff}}(I,r)}{dI}\exp\left(\frac{-2x^2}{\omega^2}\right)\right], \end{aligned} \tag{13}$$

where x is interchangeable with y. Equation (13) means the force is negative, and molecular motion is pushed toward the

high-intensity region of the laser beam focus. The parameter $\frac{d\bar{\alpha}_{\rm eff}}{dI}$ is the change in effective polarizability with intensity for linearly or circularly polarized light. Equation (13) contains both the alignment and center-of-mass motion terms which result from the ac Stark shift. The molecular alignment occurs from the $\bar{\alpha}_{\rm eff}(I,r)$ term, while the center-of-mass motion results from the spatial gradients of $I(r)$ and $\bar{\alpha}_{\rm eff}(I,r)$. By replacing $\bar{\alpha}_{\rm eff}(I,r)$ with the isotropic polarizability of the molecule $\alpha_{\rm av}$ ($\frac{d\bar{\alpha}_{\rm eff}}{dI}=0$), Eq. (13) reduces to the form used in similar studies of the dipole force [5,6,9] where no alignment is observed. The lack of molecular alignment in these studies is most likely due to the use of unseeded lasers where the optical field is subject to rapid intensity modulation due to mode beating. Injection seeding suppresses intensity spikes within the nanosecond pulse duration of the Q-switched laser, allowing coherent alignment of the molecules. The contribution of the $\frac{d\bar{\alpha}_{\rm eff}}{dI}$ term to the dipole force depends on the rotational temperature and on the intensity. For a rotational temperature of 35 K, shown in Fig. 2 at an intensity of 5.7×10^{11} W cm^2, the $\frac{d\bar{\alpha}_{\rm eff}}{dI}$ term in Eq. (13) adds an additional 10% to the total dipole force for linearly polarized light. The dipole force component arising from the spatial gradient of the effective polarizability $\nabla[\bar{\alpha}(I,r)]$ is greater for linearly polarized light as the effective polarizability is larger than that for circularly polarized light.

By solving the classical equations of motion for a group of particles in the IR field, the induced velocity change determined from Eq. (13) is compared with our experimental data.

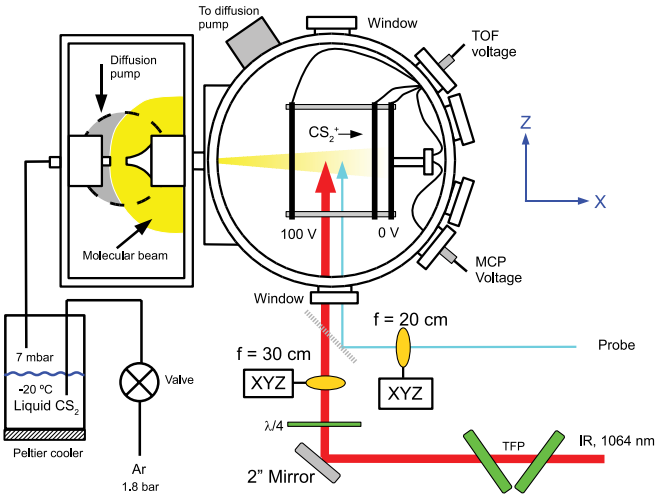

FIG. 4. (Color online) A schematic of the apparatus to measure the acceleration and deceleration of CS_2. The speed of the molecules is recorded by the TOFMS. As the IR beam is scanned along the x direction, the induced velocity change for linearly and circularly polarized light is recorded. The probe beam wavelength is $\lambda=477.93$ nm, which corresponds to the $(3+1)$ resonance-enhanced multiphoton ionization (REMPI) transition $4p\sigma(^1\Pi_u)\leftarrow\tilde{X}^1\Sigma_g^+$. The IR beam is passed through two thin-film polarizers to ensure linearly polarized light. Before being focused into the main chamber, the beam encounters a $\lambda/4$ wave plate which is used to switch between linearly and circularly polarized light.

III. EXPERIMENT

A. Apparatus

The role of molecular alignment on the dipole force was measured by recording the induced velocity imparted to carbon disulfide molecules for two different field polarizations. As shown in Fig. 4, cold CS_2 molecules are produced in a molecular beam and intersected by a focused IR and probe laser beam inside a TOFMS. A dichroic mirror, indicated by a dashed line on Fig. 4, is used to combine the IR and probe beams outside the vacuum chamber so that they are parallel and copropagating. A Spectra Physics Quanta Ray Nd:YAG (yttrium aluminum garnet) ($\lambda=1064$ nm) laser operated at 10 Hz was used to create the nonresonant optical field. This laser was injection seeded and Q-switched which provided a smooth temporal profile of 15 ns (FWHM) duration. The IR laser beam was passed through a $\frac{\lambda}{4}$ wave plate and then through a 30 cm planoconvex lens to form a Gaussian focus with an e^{-2} width of 20 μm measured on a charge-coupled device (CCD) of pixel size 5.6 μm. The Nd:YAG laser had a linear polarization of better than 1 part in 10^4, which was achieved by passing it through two thin-film polarizers. The IR pulse energy for linearly polarized light was 150 ± 5 mJ. At this energy, no ions were recorded by the MCP when the probe beam was turned off, indicating the IR laser was below the ionization threshold for the molecules. When required, the IR field polarization was converted to circular polarization by rotating the angle on the $\frac{\lambda}{4}$ wave plate by 45°. The IR pulse energy dropped by 6% in the interaction region after passage through all optics when changing from linear to circular polarization. This is consistent with differential Fresnel reflection losses between the orthogonal components of the circularly polarized laser beam when it encounters the back of the dichroic mirror which is at 45° to the incident IR beam. This effect changes the beam so that it is slightly elliptically polarized. If a molecule is completely aligned with the field polarization vector, and one of the electric-field components of circularly polarized light is reduced by 6%, the difference in maximum effective polarizability between the slightly elliptical circularly polarized beam and a perfectly circularly polarized beam is <3%. In reality, complete alignment is not realistic which reduces the difference in effective polarizability between the near circularly polarized and perfectly circularly polarized beams further. It is important, however, to correct for the overall IR intensity being 6% lower.

The probe beam was provided by a Continuum ND6000 tunable dye laser pumped by the frequency tripled output of an unseeded Q-switched Continuum Precision II 8000 Nd:YAG laser. After passage through all optics, a probe beam pulse energy of 0.2 ± 0.05 mJ was recorded entering the vacuum chamber. This was sufficient to ionize the CS_2 molecules from the ground state at a wavelength of $\lambda=477.93$ nm, which corresponds to the $(3+1)$ resonance-enhanced multiphoton ionization (REMPI) transition $4p\sigma(^1\Pi_u)\leftarrow\tilde{X}^1\Sigma_g^+$ [36,37]. The excess energy above the 10.08 eV [38] ionization potential of CS_2 is 0.28 eV. This excess energy is spread between the ejected electron and the ion. We estimate a maximum recoil velocity of 2.2 m s^{-1} imparted to the molecules for this excitation scheme. During ionization, electrons are preferentially ejected along the probe laser polarization axis, which is vertically polarized along the y axis and perpendicular to the molecular beam axis. On average, if many recordings are

taken, the net effect will be zero, as there is equal probability of an upward and downward electron emission and on average the ion velocity should be unaffected.

The IR and probe beams are focused onto the x-y plane inside the TOFMS, illustrated in Figs. 3 and 4. When the probe beam creates the CS_2^+ ions, they are repelled by the 100 V plate and collected at the MCP which is operated at -2.5 kV. We record the induced velocity change imparted onto the neutral molecules by recording the TOF of the ions. The measured TOFs of the ions agree within 1% of that predicted from numerical simulation using the software package SIMION [39]. The spectrometer plates are separated by 50 mm, and the field-free drift region is 35 mm long. The mass and velocity resolution of our mass spectrometer at the mass of interest are <1 amu and <0.5 m s^{-1}. A 300 μm slit is placed over the MCP collector plate in order to limit ion collection to just below the Rayleigh range of the probe beam. In the x-y plane, a probe beam waist radius of ≈ 5 μm was measured, and at the Rayleigh range this is increased to ≈ 7 μm. Despite having a collection region spanning the Rayleigh range (along z) and the possibility of ionizing molecules within a cross-sectional area (x-y plane) up to a width $\omega \approx 7$ μm, we estimate the spatial resolution of our probe beam to be better than 5 μm because the ionization process requires the absorption of four photons, which is most likely in the central most intense part of the probe beam focus. The spatial resolution was confirmed to be sufficient by spatially and temporally overlapping the IR and probe beams. The resulting ion signal from the probe beam is greatly decreased because of the IR beam Stark shifting the molecules out of resonance with the probe beam. By measuring the decrease in ion signal as a function of position by scanning the IR beam along the x axis through the probe beam, the shape of the IR beam was mapped out. A smooth spatial IR profile was measured indicating a good quality Gaussian focused beam. The IR beam has a large Rayleigh range (>1 mm), and the length bounded by the 300 μm slit centered at $z = 0$ means that the molecules within this range will effectively experience a constant intensity along z. The molecular beam is operated in two modes, the first uses a pressure 450 mbar (20%) of CS_2 in the pulsed valve backing chamber, while the second mode uses 7 mbar (4%) of CS_2. Both mixtures are mixed with 1800 mbar of argon. A pulsed valve with an orifice of 500 μm creates the molecular beam in a source chamber. The molecules are skimmed by a circular 2 mm orifice and enter the main chamber, which is held below 4×10^{-7} mbar during molecular beam operation. The molecular beam velocity was calculated to be ≈ 490 m s^{-1} for the 20% concentration of CS_2 and measured to be 537 ± 22 m s^{-1} for the 4% CS_2 beam concentration. The timings of the molecular beam and both lasers were controlled by two Stanford Research Systems delay pulse generators (DG535).

B. Laser polarization dependence of the dipole force

To measure the velocity change imparted to the molecules by the dipole force, we ionize the neutral molecules and measure their TOF. To avoid a decrease in the ion signal caused by the IR beam Stark shifting the molecules out of resonance with the probe beam, the probe beam was delayed by 70 ns. TOF measurements across the spatial profile of the IR beam were made by moving the IR field along the x axis while keeping the probe beam fixed. This ensures that any change in the TOF is due only to the variation in dipole force. The TOF measurements were recorded using a 1200 shot average of the TOF spectrum. The induced velocity change is subsequently determined by converting the change in TOF to a change in velocity.

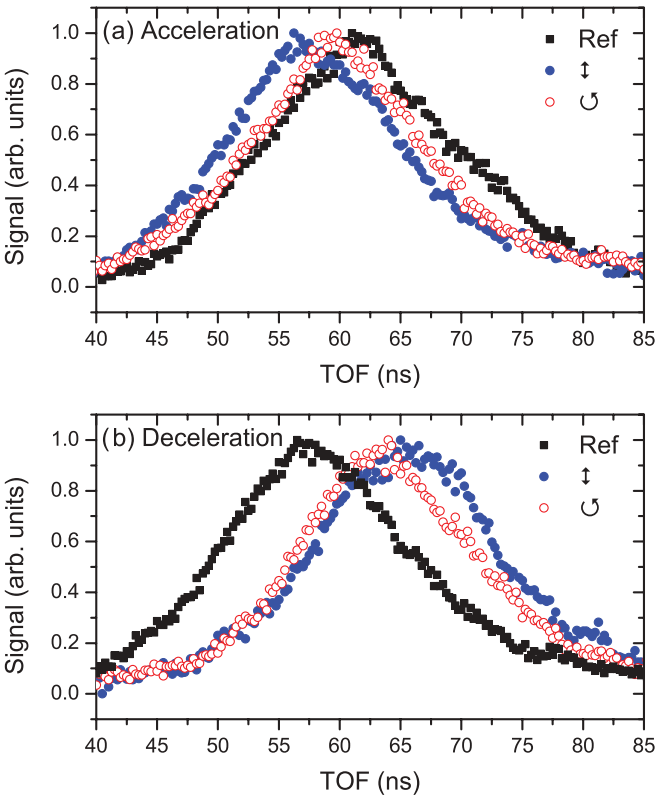

FIG. 5. (Color online) The normalized time-of-flight spectra are shown when the $x = -10$ and $x = +10$ μm positions are probed. (a) Shows the time-of-flight spectrum recorded using 100 V on the repeller plate in the TOFMS for CS_2 molecules at $x = -10$ μm. This position corresponds to acceleration of the molecules. The filled circles are the TOF spectra due to LPL and the filled squares are the TOF spectrum for CPL. The open circles in both (a) and (b) are the unperturbed TOF spectra when the IR field is switched off. It can be seen in (a), the IR field has accelerated the molecules and so they arrive earlier at the detector. The opposite is true for (b), recorded at $x = +10$ μm, where deceleration of the molecules means that it takes longer for them to arrive at the detector. These data were recorded using 70 V on the repeller electrode in the TOFMS. In both acceleration and deceleration, it is clear that LPL exerts a greater dipole force than CPL.

Figure 5 shows the normalized TOF spectra measured near $x = 10$ and $x = -10$ μm. These are positions of maximum dipole force for linearly polarized light (LPL) (blue) and near circularly polarized light (CPL) (red). The reference TOF spectra, where the IR field is off is also shown (black). In Fig. 5(a), the TOF spectra were recorded at $x = -10$ μm where acceleration of the CS_2 molecules is clearly seen in the TOF spectra. Both LPL and near CPL TOF spectra arrive earlier at the mass spectrometer compared to the reference trace. Also obvious is the difference in arrival time between LPL and CPL, indicating the dipole force is greater for linearly

polarized light. In Fig. 5(b), the $x = 10\ \mu$m position is probed, and the molecules are decelerated as they travel away from the IR field. This is shown in the TOF for LPL and near CPL arriving at a later time compared to the reference trace. Again there is a measurable difference between the arrival times of LPL and near CPL. To calculate the induced velocity change, we use a TOF dispersion that is defined to be the change in TOF to the change in velocity which was calculated using SIMION software. This ratio has an error of ±3% based on our TOF measurements. The dispersion values are 0.4 ns/(m s^{-1}) and 0.7 ns/(m s^{-1}) for the 100 and 70 V settings used on the repeller electrode in the mass spectrometer. These electrode voltages correspond to the spectra shown in Figs. 5(a) and 5(b), respectively. The measured induced velocity changes are equivalent and are not affected by the use of different voltages on the electrode. Using the dispersion ratio and the TOF of each laser polarization, obtained using a Gaussian fit, the measured induced velocity change for LPL and near CPL from Fig. 5 is (9.6 ± 0.6) m s^{-1} and (4.7 ± 0.5) m s^{-1}, respectively, for acceleration and (10.6 ± 0.6) m s^{-1} and (8.2 ± 0.6) m s^{-1}, respectively, for deceleration. The errors arise from the velocity resolution of the mass spectrometer and the error in the dispersion ratio. These measurements do not take into account the 6% drop in optical intensity for near CPL, but it can be seen that the velocity change in both acceleration and deceleration is greater than 6%.

The induced velocity change for each TOF spectrum, recorded along the x axis through the IR focus using LPL and near CPL, is plotted in Fig. 6(a). The experiment was repeated three times and averaged, with the error bars resulting from the average difference between successive scans. Figure 6(a) shows the shape of the resulting velocity shift versus position for both polarizations. It also shows that the molecules are forced to the center of the IR beam. The profile is proportional to the gradient of a Gaussian beam, which is consistent with previous measurements [6,9]. Second, LPL (blue solid circles) clearly exerts a greater dipole force than does near CPL (red open circles). The data for the near CPL has not been corrected for the 6% drop in intensity caused by the Fresnel loss at the dichroic mirror. The solid lines are theoretical fits to the data and are calculated as follows. The induced velocity shift depends strongly on the intensity of the laser field and on the rotational temperature of the molecules. The measured spatial and temporal profiles of the focused beam in the interaction region yield peak intensities of $(7.6 \pm 2.3) \times 10^{11}$ and $(7.1 \pm 2.2) \times 10^{11}$ W cm^{-2} for linearly and near circularly polarized light. We reduce the uncertainty in intensity by repeating the experiment using the molecular beam seeded with 20% CS_2. Under these conditions the rotational temperature is sufficiently high such that no alignment is observed. This is shown in Fig. 6(b), where LPL and near CPL have no clear difference in dipole force. From Fig. 6(b), the averaged velocity shift due to the dipole force is 7.5 m s^{-1}. Using Eq. (13), a fitted curve based on the average polarizability of CS_2 with α_{av} and $\frac{d\bar{\alpha}_{eff}}{dI} = 0$, produces an intensity of $(5.7 \pm 0.3) \times 10^{11}$ and $(5.4 \pm 0.3) \times 10^{11}$ W cm^{-2} for LPL and near CPL, respectively. Both intensities are within the experimental error of the intensity measurements made using the CCD and photodiode. With the uncertainty in intensity reduced to ±5%, the fit to the LPL and near

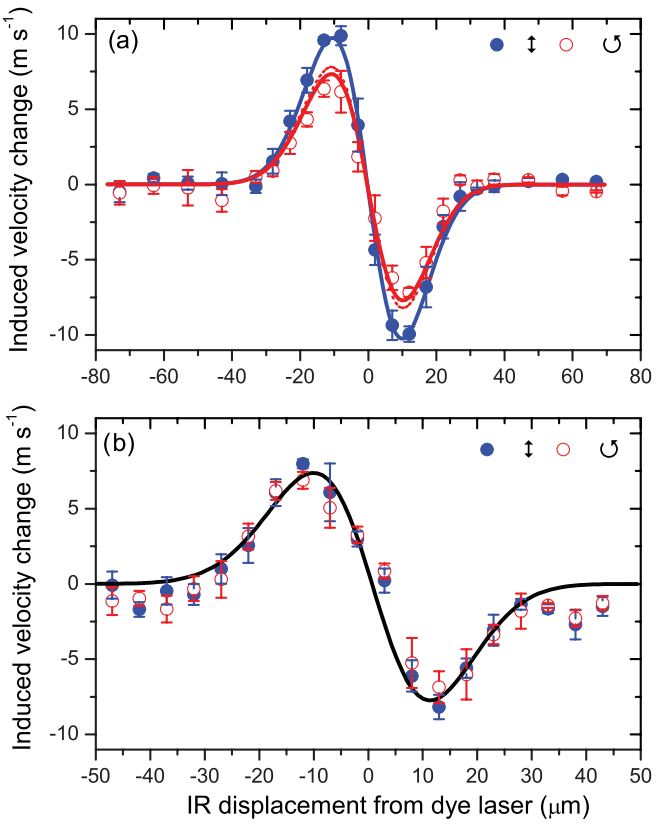

FIG. 6. (Color online) (a) The difference in each TOF spectra converted to velocity and plotted as a function of position in the x direction through the IR focus using the 5% CS_2 beam. The solid lines are fits based on a rotational temperature of 35 K with $I_0 = 5.7 \pm 0.3 \times 10^{11}$ and $I_0 = 5.4 \pm 0.3 \times 10^{11}$ W cm^{-2} for LPL and CPL, respectively (see text). (b) Under the same experimental conditions, the experiment was repeated but using the 20% CS_2 seeded molecular beam, the solid line is a fit based on α_{av}. For both (a) and (b), the induced velocity changes for LPL (filled circles) and CPL (open circles) were recorded and averaged over three scans.

CPL data points in Fig. 6(a) are achieved by holding the alignment-dependent dipole force equation at the new intensity and varying the rotational temperature. This produces a best fit of 35 K, the fitting range and uncertainty in intensity mean the temperature could be as low as 33 K or as high as 45 K. The solid lines in Fig. 6(a) show the numerical predictions from Eq. (13) at the stated temperature and intensity for each polarization. Also shown on Fig. 6(a) is a dashed line (red) which shows the induced velocity change if the LPL and near CPL beams have the same intensity. As this dashed curve is separated quite clearly from the LPL curve, this shows there is a clear difference in the dipole force between LPL and CPL purely due to molecular alignment.

Using the solid curves, the maximum change in velocity imparted to the molecules is 9.8 and 7.3 ms^{-1} in acceleration and 10.0 and 7.6 m s^{-1} in deceleration. The corresponding effective polarizability at 35 K is 11.4×10^{-40} C m^2 V^{-1} with $\langle \cos^2 \theta_l \rangle = 0.49$ for linearly polarized light and 10.0×10^{-40} C m^2 V^{-1} with $\langle \cos^2 \theta_c \rangle = 0.28$ for circularly polarized light. The average polarizability of a CS_2 molecule that is not aligned by the field is 9.7×10^{-40} C m^2 V^{-1} with $\langle \cos^2 \theta_{l,c} \rangle = \frac{1}{3}$. The well depths of the optical Stark potential

for the linearly and near circularly polarized fields are 89 and 74 K, respectively. This produces a 25% change in the dipole force and a 20% change for equal beam intensities. Additionally, because the effective polarizability is now dependent on the intensity of the laser field, the dipole force is no longer directly proportional to $\nabla I(r)$. This is demonstrated by the fact that the difference in effective polarizability between the laser polarizations is only 12%, while the change in the dipole force is 20%.

The maximum velocity change in these types of experiments is typically limited by the ionization threshold of the molecules. In the dipole experiments described in this paper, the IR laser was operated just below the ionization threshold for LPL and held at that intensity. The ionization threshold is higher for CPL than for LPL, and so if desired, the CPL intensity could be increased, thereby yielding larger induced velocity shifts.

C. Elliptically polarized light

Figure 7 shows the induced velocity change imparted to the molecules as a function of $\frac{\lambda}{4}$ wave-plate angle. The measurements were taken at the $x = -10$ μm position, where maximum acceleration along the x axis occurs. The same IR intensity described in the previous section was used. The molecular beam seeded with 4% CS_2 was used. In Fig. 7, near CPL occurs at 96° and 186°, while LPL occurs at 141°. Each data point is an average of two scans. The error bars are caused by the velocity resolution of the mass spectrometer and the difference between averaged measurements. The IR pulse energy was recorded for each data point and was used to remove the intensity dependence arising from the 6% difference in optical intensity between LPL and near CPL. The solid line (red) is a fit to the data as a function of wave-plate angle and has the form

$$\Delta v(\psi) = \Delta v_c + A\cos^2(2\psi), \tag{14}$$

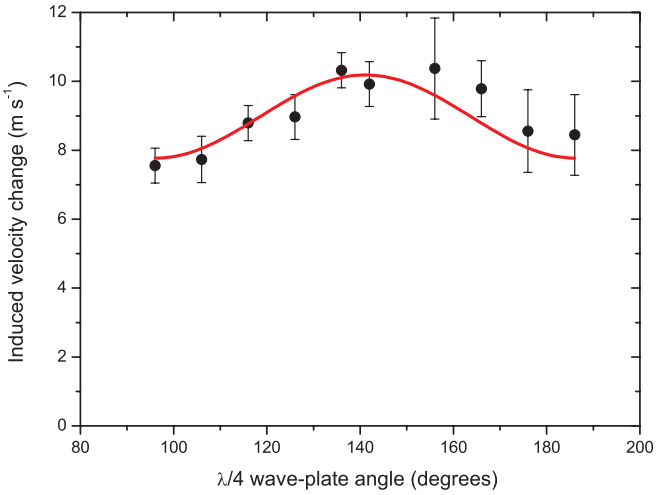

FIG. 7. (Color online) Induced velocity change as a function of $\frac{\lambda}{4}$ wave-plate angle. Each data point is an average of two scans taken at $x = -10$ μm, corresponding to acceleration of the molecules. The solid line shows a fit based on the induced velocity change as a function of wave-plate angle.

where $\Delta v(\psi)$ is the induced velocity shift due to an angle ψ between the electric-field vector of LPL and the optical axis of the $\frac{\lambda}{4}$ wave plate. The fitting constants are Δv_c and $A = \Delta v_l - \Delta v_c$, where Δv_l and Δv_c are the induced velocity shifts at the $x = -10$ μm position for linearly and circularly polarized light, respectively. When $\psi = 0°$ and $\psi = 45°$, Eq. (14) produces the induced velocity shift for LPL and CPL, respectively. By fitting to the data, the constants Δv_c and A were determined and yielded the values $\Delta v_c = 7.8 \pm 0.2$ m s^{-1} and $\Delta v_l = 10.2 \pm 0.4$ m s^{-1}, in good agreement with the data shown in Fig. 6.

D. Molecular lens

Although we have measured the induced velocity along the molecular beam direction, the same forces are also produced in any radial direction in the x-y plane. The force in the y direction acts as a cylindrical lens for the molecules [5,8] (see Fig. 3). This molecule-optical lens is, however, different from a conventional optical lens because it is only turned on for a short time (15 ns), and therefore only molecules that are initially in the field during the optical pulse will be focused. As a larger force is created for LPL, molecules will focus closer to the IR beam when compared to near CPL. To verify this, we have measured the relative density of molecules as they are focused downstream for both polarizations. These results are shown in Fig. 8 as a function of the distance between the center of the IR focus and the ionization probe beam. For each IR-probe beam separation, we adjust the temporal delay between the firing of the IR and probe laser to maximize the measured density. We define the distance between the center of the IR beam and probe beam where the peak density is measured to be the focal length of the molecular-optical lens. Figure 8 indicates that a shorter focal length (≈600 μm) is produced for LPL when compared to a focal length of ≈700 μm for near CPL. If we assume that the focal length of the

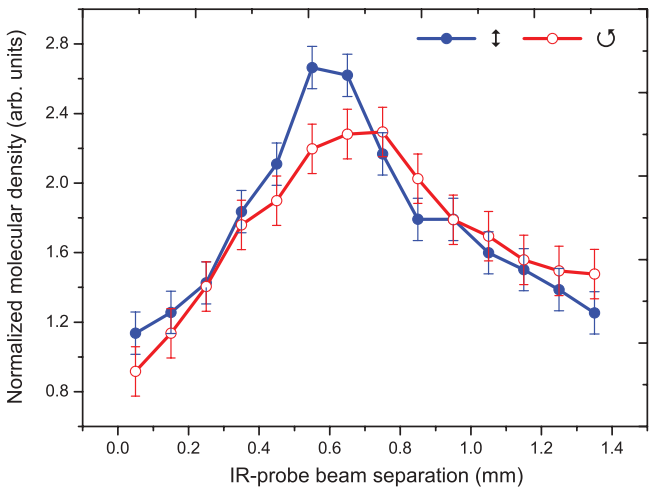

FIG. 8. (Color online) Molecular density in the focal region of the molecular optical lens. The downstream density along the x axis is determined by measuring the ionization signal as a function of distance between the IR and probe beams. LPL (filled circles) produces a molecular optical lens with a focal length of 600 μm; CPL (open circles) produces a focal length of 700 μm.

molecular-optical lens is inversely proportional to the dipole force, we would expect a difference in focal length of 80 μm rather than our measured value of 100 μm in Fig. 8 if equal intensity beams were used. This is because for equal intensity beams, a difference of 20% was determined in Fig. 6. Thus, although the optical intensity is slightly less for near CPL, we can still attribute a large portion of the difference in focal length to be due to molecular alignment of the molecules. The numerical aperture of a conventional optical lens is $\approx D/2f$, where D is the lens diameter and f is the focal length. A larger numerical aperture produces a smaller focused spot as well as a higher on-axis intensity. Thus, our cylindrical lens has a higher numerical aperture for LPL than for near CPL, because its focal length is shorter and we should expect a smaller molecular focus and therefore a higher density. This effect can be seen in Fig. 8 where the peak density, normalized to the background-gas density, is 21% larger for the linearly polarized case than for the near circularly polarized beam, indicating that the spot size is smaller by approximately the same amount.

IV. VIBRATIONAL ac STARK EFFECT

We have so far only considered the effect of the dipole force on CS_2 molecules in their electronic and vibrational ground state. A molecule in an excited vibrational state within an electric field can change the magnitude of the induced Stark shift because the averaged geometry of the nuclear motions can change the components of the static polarizability tensor [40–42]. The effect of vibrations on the ac Stark shift is important, because vibrational cooling in molecular jets is inefficient and can often remain in a room temperature distribution [43,44]. If molecules which are vibrating exhibit different behavior than that of ground-state molecules, they would introduce additional abberations into a molecule-optical lens.

Figure 9(a) shows the integrated signal from ionized CS_2 molecules in our molecular beam as a function of probe laser beam wavelength in the range 477–484 nm. It shows two electronic resonances: $4p\sigma(^1\prod_u)0_0^0 \leftarrow \tilde{X}^1\sum_g^+$, which was used in the alignment-dependent dipole force study, and another electronic resonance corresponding to the transition $4p\sigma(^3\prod_u)0_0^0 \leftarrow \tilde{X}^1\sum_g^+$. Three vibrational resonances are identified as part of the $4p\sigma(^1\prod_u) \leftarrow \tilde{X}^1\sum_g^+$ band and are labeled 2_1^1, 2_2^2, 2_3^3. The integer 2 denotes the degenerate bending mode, the superscript is the vibrational quantum number in the excited state, and the subscript is the quantum number in the lower state. The label ν_2 is often used to indicate the quantum number of the degenerate bending mode vibrational state [45]. Thus, in all of the vibrational transitions recorded, there is only a change in electronic state, and the molecule remains in the same vibrational state. The strengths of the vibrational transitions can be used to approximate a vibrational temperature [36,46]. In our molecular beam we have estimated the vibrational temperature for both 4% and 20% CS_2 mixtures seeded in argon to be 250 ± 14 and 298 ± 7 K, respectively. These temperatures are within the error range for the temperature of the CS_2 reservoir in each mode of operation. This suggests there is actually no vibrational cooling in our molecular beam. At the quoted vibrational temperatures, the fraction of molecules in the 2_1^1 state is 0.16 ± 0.02 and 0.21 ± 0.01 for the 4% and 20% CS_2 molecular beams, respectively.

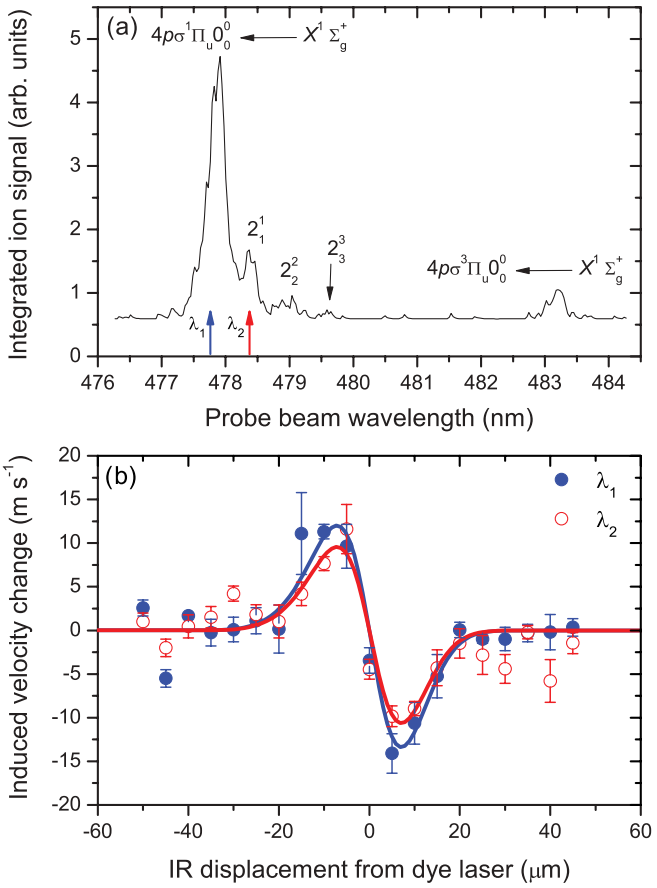

FIG. 9. (Color online) (a) REMPI excitation scan of the CS_2 from 476.3 to 484.3 nm. The electronic and vibrational states are indicated. The arrows indicate the wavelength of the 0_0^0 and 2_1^1 transitions used in the experiment. (b) The difference in induced velocity of each TOF for both the ground state (filled circles) and $\nu_2 = 1$ (open circles) state is shown between subsequent positions along x. The solid lines indicate simulated data with $I_0 = 7.3 \times 10^{11}$ W cm^{-2} with an e^{-2} waist radius of 13 μm. The fitted polarizability of the $\nu_2 = 1$ state is $\alpha_{\rm av}^{\nu} = (7.7 \pm 2.2) \times 10^{-40}$ C m^2 V^{-1}.

In an experiment almost identical to that for measuring the alignment-dependent dipole force in Sec. III B, the acceleration and deceleration of the ground state can be compared with the vibrational bending mode in CS_2 in order to determine if there is a difference in polarizability between the states. The signal strength of the 4% beam was too low to be used, so we use the 20% CS_2 beam and the approximate molecule's polarizability can be represented by an average $\alpha_{\rm av}$ and $\alpha_{\rm av}^{\nu}$ for the ground and vibrational states respectively. The translational temperature of the ground- and excited-state molecules was measured to be 12.7 ± 0.9 and 10.6 ± 0.8 K, respectively. The experiment was carried out identically as in Sec. III B except at each increment of x, instead of changing between LPL and CPL, the wavelength of the probe beam was changed. The arrows on Fig. 9(a) show the wavelengths used by the probe beam with $\lambda_1 = 477.93$ and $\lambda_2 = 478.45$ nm, corresponding to

ionization via the 0_0^0 and 2_1^1 transitions, respectively. A slightly higher IR pulse energy and smaller IR spot size were used in the experiment; our photodiode and CCD measurements yielded a peak intensity of $I_0 = (9.2 \pm 2.8) \times 10^{11}$ W cm^{-2}. Figure 9(b) shows the induced velocity change for both the 0_0^0 (blue) and 2_1^1 (red) transitions as the IR beam is traversed along the x axis using only linearly polarized light. The experiment was repeated three times with the error bars resulting from the average difference between data points. Both the ground state and $\nu_2 = 1$ vibrational state show the characteristic acceleration and deceleration induced at the $x = \pm\frac{\omega}{2}$ positions, indicating the shape of the dipole force along x for the $\nu_2 = 1$ state is similar to that shown in Sec. III B. The solid lines in Fig. 9(b) indicate the predicted dipole force from Eq. (13), where α_{av} (blue) has been used with $\frac{d\alpha_{\text{eff}}}{dI} = 0$ to fit to the ground-state data. The fitted intensity to both curves is 7.3×10^{11} W cm^{-2}, which is within the experimental error of the photodiode and CCD measurements.

After determining I_0 by fitting to the ground-state data, the $\nu_2 = 1$ data are fitted by varying the average polarizability α_{av}^{ν}. The best fit is $\alpha_{\text{av}}^{\nu} = (7.7 \pm 2.2) \times 10^{-40}$ C m^2 V^{-1} which is within the error range of the ground-state polarizability α_{av}. Although the same averaging times were used as for the data recorded in Fig. 6, the large amount of error arises from two sources: the spread of points outside of the IR region which should have a zero velocity shift and the smaller IR spot size. A smaller waist radius for the IR focus leads to larger errors because the induced velocity shift is more sensitive to errors in horizontal position. A combination of IR laser pointing stability and translation stage accuracy can create this error. Additionally, in the regions where no field is applied ($x < -30\,\mu$m and $x > 30\,\mu$m) and where the induced velocity change should be zero, the vibrational state shows large scatter in the measured induced velocity. This is most likely to be due to the small signal from the 2_1^1 transition in the TOF spectra. Also, as the molecule is being placed in a strong nonresonant field, this may alter the vibrational frequency of the bending mode and the averaged geometry of the molecule, which could alter the average polarizability. This effect has not been considered in our study. With an experimentally determined value of $\alpha_{\text{av}}^{\nu} = (7.7 \pm 2.2) \times 10^{-40}$ C m^2 V^{-1}, we conclude that the errors are too large to sufficiently resolve a difference in the polarizability of the bending mode.

This effect could be further explored with greater sensitivity using an optical lattice [47–49]. Where a larger gradient leads to a larger dipole force and larger induced velocity changes. In addition, less time would be required to acquire data, which would reduce requirements on the stability of the experiment over time. An optical lattice experiment is formed by two counterpropagating laser beams to create a standing wave. The molecular beam travels perpendicular to the direction of the standing wave. The maximum well depth for linearly polarized light using a single focused Gaussian beam under the conditions described above is 97 K, while using the same intensity, a periodic lattice potential could exert a maximum well depth of 388 K, four times that of a single focused Gaussian beam. Although the same well depth could be obtained using a single Gaussian beam by increasing the intensity, the maximum value of I_0 is limited by the ionization threshold of the molecules. The resulting spatial gradient of the standing wave potential is much greater than a focused Gaussian beam and would allow this technique to be much more sensitive to changes in molecular mass or polarizability. A difference in polarizability due to a different averaged geometry might also be more pronounced if molecules of higher vibrational energy were used. Additionally, a molecule containing isotopes may enhance this effect. For example, $C^{34}S^{32}S$ is 2 atomic units heavier than CS_2 and has a natural abundance of 7.9%.

V. CONCLUSION

We have measured the effect of laser-induced molecular alignment on the dipole force for CS_2 molecules. To accomplish this we have measured the velocity change induced by a pulsed nanosecond, nonresonant laser field. Using this scheme we have measured a 20% change in the peak velocity imparted to molecules via the dipole force using light fields from linearly to circularly polarized light. We show two effective polarizabilities are created for linear and circular laser polarization, and subsequently a dipole force of different magnitude is created for the same molecular species. The effect of elliptically polarized light on the dipole force was examined, and it was shown the dipole force could be smoothly altered between linearly and circularly polarized light cases. Using a molecule-optical lens, our measurements have shown that the downstream molecular density and focal length could be altered by changing the laser field polarization. The influence of an occupied $\nu_2 = 1$ vibrational level was also investigated and compared against ground-state CS_2 molecules. The shape of the dipole force versus distance through the IR focus was found to have the same general shape as the ground-state molecules. However, the experiment lacked sufficient resolution to conclusively show a difference between the states.

Our measurements on molecular alignment and its effect on the dipole force demonstrate that laser-induced alignment can be used to modify the magnitude of the dipole force. This process is unique to the manipulation of the center-of-mass motion of molecules and will be useful for tailoring the dipole force in molecular optics applications such as the creation of cold molecules by Stark deceleration, the focusing of molecules onto surfaces, and molecular separation schemes based on polarizability-to-mass ratio. Since alignment, and therefore the force that can be applied to a particular molecule, is dependent on the rotational state, the variation of dipole force with rotational state could be used for rotational-state selection of nonpolar molecules in the same vibrational state and may be complementary to recent experiments that have used an electrostatic field to change the center-of-mass motion of polar molecules while using laser-induced alignment to induce a very high degree of alignment and orientation [50,51].

ACKNOWLEDGMENTS

We would like to acknowledge useful discussions with J. Underwood and support from the UK Engineering and Physical Sciences Research Council.

[1] J. E. Bjorkholm, R. R. Freeman, A. Ashkin, and D. B. Pearson, Phys. Rev. Lett. **41**, 1361 (1978).

[2] T. Weber, J. Herbig, M. Mark, H.-C. Nägerl, and R. Grimm, Science **299**, 232 (2003).

[3] T. Kinoshita, T. Wenger, and D. S. Weiss, Science **305**, 1125 (2004).

[4] H. T. Bookey, M. N. Shneider, and P. F. Barker, Phys. Rev. Lett. **99**, 133001 (2007).

[5] B. S. Zhao, S. H. Lee, H. S. Chung, S. Hwang, B. Friedrich, and D. S. Chung, J. Chem. Phys. **119**, 8905 (2003).

[6] H. Stapelfeldt, H. Sakai, E. Constant, and P. B. Corkum, Phys. Rev. Lett. **79**, 2787 (1997).

[7] H. Sakai, A. Tarasevitch, J. Danilov, H. Stapelfeldt, R. W. Yip, C. Ellert, E. Constant, and P. B. Corkum, Phys. Rev. A **57**, 2794 (1998).

[8] H. S. Chung, B. S. Zhao, S. H. Lee, S. Hwang, K. Cho, S. Shim, S. Lim, W. K. Kang, and D. S. Chung, J. Chem. Phys. **114**, 8293 (2001).

[9] B. S. Zhao *et al.*, Phys. Rev. Lett. **85**, 2705 (2000).

[10] R. Fulton, A. I. Bishop, and P. F. Barker, Phys. Rev. Lett. **93**, 243004 (2004).

[11] J. P. Heritage, T. K. Gustafson, and C. H. Lin, Phys. Rev. Lett. **34**, 1299 (1975).

[12] L. Fonda, N. Mankoc, and M. Rosina, Nuovo Cimento **7**, 437 (1986).

[13] J. G. Underwood, B. J. Sussman, and A. Stolow, Phys. Rev. Lett. **94**, 143002 (2005).

[14] J. J. Larsen, K. Hald, N. Bjerre, H. Stapelfeldt, and T. Seideman, Phys. Rev. Lett. **85**, 2470 (2000).

[15] F. Rosca-Pruna and M. J. J. Vrakking, Phys. Rev. Lett. **87**, 153902 (2001).

[16] J. Itatani, J. Levesque, D. Zeidler, H. Nikura, H. Pépin, J. Kieffer, P. B. Corkum, and D. M. Villeneuve, Nature **432**, 867 (2004).

[17] T. P. Rakitzis, A. van den Brom, and M. H. M. Janssen, Science **303**, 1852 (2004).

[18] B. J. Sussman, D. Townsend, M. Y. Ivanov, and A. Stolow, Science **314**, 278 (2006).

[19] C. B. Madsen, L. B. Madsen, S. S. Viftrup, M. P. Johansson, T. B. Poulsen, L. Holmegaard, V. Kumarappan, K. A. Jørgensen, and H. Stapelfeldt, Phys. Rev. Lett. **102**, 073007 (2009).

[20] H. Sakai, C. P. Safvan, J. J. Larsen, K. M. Hilligsøe, K. Hald, H. Stapelfeldt, and T. Seideman, J. Chem. Phys. **110**, 10235 (1999).

[21] S. M. Purcell and P. F. Barker, Phys. Rev. Lett. **103**, 153001 (2009).

[22] B. J. Sussman, J. G. Underwood, R. Lausten, M. Y. Ivanov, and A. Stolow, Phys. Rev. A **73**, 053403 (2006).

[23] B. W. Shore, *The Theory of Coherent Atomic Excitation*, Vol. II (Wiley, New York, 1990).

[24] T. Seideman, J. Chem. Phys. **107**, 10420 (1997).

[25] J. D. Graybeal, *Molecular Spectroscopy* (McGraw-Hill, New York, 1988).

[26] G. Herzberg, *Molecular Spectra and Molecular Structure III: Electronic Spectra and Electronic Structure of Polyatomic Molecules* (Van Nostrand Reinhold, New York, 1966).

[27] D. M. Brink and G. R. Satchler, *Angular Momentum* (Clarendon, Oxford, 1993).

[28] A. R. Edmonds, *Angular Momentum in Quantum Mechanics* (Princeton University, Princeton, 1996).

[29] A. D. Bandrauk, Y. Fujimura, and R. J. Gordon, *Laser Control and Manipulations of Molecules* (Oxford University, Oxford, 2002).

[30] J. Ortigoso, M. Rodriguez, M. Gupta, and B. Friedrich, J. Chem. Phys. **110**, 3870 (1999).

[31] A. BenHaj-Yedder, A. Auger, C. M. Dion, E. Cances, A. Keller, C. LeBris, and O. Atabek, Phys. Rev. A **66**, 063401 (2002).

[32] E. Hamilton, T. Seideman, T. Ejdrup, M. D. Poulsen, C. Z. Bisgaard, S. S. Viftrup, and H. Stapelfeldt, Phys. Rev. A **72**, 043402 (2005).

[33] M. Abramowitz and I. A. Stegun, *Handbook of Mathematical Functions with Formulas, Graphs, and Mathematical Tables*, 10th ed. (National Bureau of Standards, Washington, 1972).

[34] H. Mori, T. Nimi, I. Akiyama, and T. Tsuzuki, Phys. Fluids **17**, 117103 (2005).

[35] G. Herzberg, *Spectra of Diatomic Molecules* (Academic, Orlando, 1938).

[36] J. Baker, M. Konstantaki, and S. Couris, J. Chem. Phys. **103**, 2436 (1995).

[37] R. A. Morgan, M. A. Baldwin, A. J. Orr-Ewing, M. N. R. Ashfold, W. J. Burma, J. B. Milan, and C. A. de Lange, J. Chem. Phys. **104**, 6117 (1996).

[38] C. Cossart-Magos and M. Horani, J. Chem. Phys. **104**, 7412 (1996).

[39] [www.simion.com].

[40] X. J. Gu, N. R. Isenor, and G. Scoles, Phys. Rev. A **39**, 413 (1989).

[41] W. Q. Cai, T. E. Gough, X. J. Gu, N. R. Isenor, and G. Scoles, Phys. Rev. A **36**, 4722 (1987).

[42] M. A. Morrison and P. J. Hey, J. Chem. Phys. **70**, 4034 (1979).

[43] S. Liu, Q. Zhang, C. Chen, Z. Zhang, J. Dai, and X. Ma, J. Chem. Phys. **102**, 3617 (1995).

[44] I. Fischer, A. Lochschmidt, A. Strobel, G. Nieder-Schatteburg, K. Muller-Dethlefs, and V. E. Bondybey, Chem. Phys. Lett. **202**, 542 (1993).

[45] W. Demtröder, *Laser Spectroscopy: Basic Concepts and Instrumentation* (Springer, New York, 2003).

[46] R. McDiarmid and J. P. Doering, J. Chem. Phys. **91**, 2010 (1989).

[47] R. Fulton, A. I. Bishop, M. N. Schneider, and P. F. Barker, Nature Phys. **2**, 465 (2006).

[48] P. F. Barker and M. N. Shneider, Phys. Rev. A **64**, 033408 (2001).

[49] P. F. Barker, S. M. Purcell, and M. N. Shneider, Phys. Rev. A **77**, 063409 (2008).

[50] L. Holmegaard, J. H. Nielsen, I. Nevo, H. Stapelfeldt, F. Filsinger, J. Küpper, and G. Meijer, Phys. Rev. Lett. **102**, 023001 (2009).

[51] O. Ghafur, A. Rouzée, A. Gijsbertsen, W. K. Siu, S. Stolte, and M. J. J. Vrakking, Nature Phys. **5**, 289 (2009).